Monthly Notices
of the
ROYAL ASTRONOMICAL SOCIETY

Mon. Not. R. Astron. Soc. **417,** 3061–3071 (2011) doi:10.1111/j.1365-2966.2011.19464.x

TESELA: a new Virtual Observatory tool to determine blank fields for astronomical observations

N. Cardiel,[1⋆] F. M. Jiménez-Esteban,[2,3,4] J. M. Alacid,[2,3] E. Solano[2,3] and M. Aberasturi[2,3]

[1]*Departamento de Astrofísica y CC. de la Atmósfera, Facultad de Ciencias Físicas, Avenida Complutense s/n, E-28040 Madrid, Spain*
[2]*Departamento de Astrofísica, Centro de Astrobiología (INTA-CSIC), PO Box 78, Villanueva de la Cañada, E-28691 Madrid, Spain*
[3]*Spanish Virtual Observatory, Spain*
[4]*Saint Louis University, Madrid Campus, Division of Science and Engineering, Avenida del Valle 34, E-28003 Madrid, Spain*

Accepted 2011 July 18. Received 2011 July 12; in original form 2011 May 11

ABSTRACT

The observation of *blank fields*, regions of the sky devoid of stars down to a given threshold magnitude, constitutes one of the typical important calibration procedures required for the proper reduction of astronomical data obtained in imaging mode. This work describes a method, based on the use of the Delaunay triangulation on the surface of a sphere, that allows for easy generation of blank-field catalogues. In addition to that, a new tool named TESELA, accessible through the Internet, has been created to facilitate the user to retrieve, and visualize using the Virtual Observatory tool ALADIN, the blank fields available near a given position in the sky.

Key words: methods: data analysis – methods: numerical – catalogues – virtual observatory tools.

1 INTRODUCTION

Scientific research progress is critically based on correct exploitation of data obtained at the limit of the technological capabilities. Thus, prior to data analysis and interpretation, the quality of the data treatment must be assured in order to guarantee that the information content in that data is preserved. In observational astrophysics and, in particular, imaging with ground-based telescopes, data treatment is performed following data-reduction procedures. The main goal of such reduction processes is to minimize the influence of data-acquisition imperfections on the estimation of the desired astronomical measurements (see e.g. Gilliland 1992 for a short review on noise sources and reduction processes of CCD data). For this purpose, one must perform appropriate manipulations of data and calibration frames, the latter properly planned and obtained to facilitate the reduction procedure. In this sense, image flat-fielding and sky subtraction constitute two of the most common and important reduction steps. Their relevance should not be underestimated, since inadequate flat-fielding or sky subtraction easily leads to the introduction of systematic uncertainties in the data. Contrary to random errors, which can be controlled by applying normal statistical methods, the systematic uncertainties can propagate hidden within the arithmetically manipulated data to the final measurements, where their impact may considerably bias their interpretation.

Concerning image flat-fielding, the corresponding calibration frames needed to proceed through this reduction step are typically divided into two categories: images intended to provide high-frequency-scale sensitivity variations (the pixel-to-pixel response) and images whose goal is to facilitate the removal of the two-dimensional low-frequency-scale sensitivity variations of the detectors. The former are usually obtained from continuum lamps (either within the instrument itself or by illuminating a flat screen or the inner dome of the telescope), although the colour of such lamps is not expected to match the spectral energy distributions of the science targets, and ideally dark night sky flats, obtained by pointing the telescope to a *blank field*, should be observed instead. Since this is quite expensive in terms of observing time, this approach is very rarely used. The low-frequency flat-fields are usually twilight exposures. The problem here is that the time during which the sky surface brightness is high enough to clearly overpass the signal of any star in the field of view, but not too high to saturate the frames, is placed on two time-windows every day, one at the beginning of the evening twilight and the other at the end of the morning twilight. The observational strategy typically consists of obtaining a series of images, shifting the telescope position a few arcseconds between the different exposures in order to avoid the bright stars in the field of view to appear in the same detector pixels. Those pixels are afterwards masked when combining the individual exposures during the reduction procedure. In any case, very bright stars need to be avoided since the point spread function of these objects can introduce spikes and artefacts that are not so easily removed during the reduction of the flat-field images. For this purpose, the use of *blank fields* is the best option.

Sky subtraction cannot always be performed by measuring the night sky level in the same frame where the scientific targets are

⋆E-mail: cardiel@fis.ucm.es

present. This is especially true when the target dimensions are comparable to the detector field of view. In this circumstance, separate sky frames are observed, by pointing the telescope to a position devoid of stars as much as possible. For the sky-subtraction procedure to be successful, it is essential that these separate sky images are obtained under identical observing conditions, that is, very close in time and sky position, since this is the only way to prevent varying observing conditions that modify the sky surface brightness.

From the above discussion, it is clear that the observation of sky regions devoid of stars down to a given magnitude is a very important aspect to be taken into account when carrying out astronomical observations. To date, no systematic catalogue is available, providing the location in the sky of blank fields for varying limiting magnitudes.[1] With modern instrumentation intended to be used in large imaging surveys, the problem is expected to become more demanding. The situation is also starting to be important in spectroscopic observations, since the advent of integral field units with high multiplexing capabilities (and thus increasingly larger field of view) is expected to be one of the most common instrumentations in ground-based observatories.

The work presented in this paper describes a method that helps to determine the availability of blank fields in any region of the celestial sphere, based on the use of the Delaunay triangulation. The method has been employed to generate catalogues of blank fields to varying limiting magnitudes. In order to facilitate the use of these catalogues, we have created TESELA, a new tool accessible through the Internet, which provides a simple interface that allows the user to retrieve the list of blank fields available near a given position in the sky.

Section 2 of this paper describes the method and presents some statistical analysis of its application to the Tycho-2 (Høg et al. 2000) catalogue. Section 3 describes the new tool TESELA. A detailed description of the tessellation of sky subregions is presented in Appendix A.

2 TESSELLATING THE SKY

2.1 The Delaunay triangulation

The Delaunay triangulation (Delaunay 1934) is a subdivision of a geometric object (e.g. a surface or a volume) into a set of simplices. A simplex, or n-simplex to be specific, is an n-dimensional analogue of a triangle. More precisely, a simplex is the convex hull (convex envelope) of a set of $(n + 1)$ points.

In particular, for the Euclidean planar (two-dimensional) case, given a set of points, also called nodes, the Delaunay triangulation becomes a subdivision of the plane into triangles, whose vertices are nodes. For each of these triangles, it is possible to determine their associated circumcircle, the circle passing exactly through the three vertices of a triangle, and whose centre, the circumcentre, can easily be computed as the intersection of the three perpendicular bisectors. Interestingly, in a Delaunay triangulation, all the triangles satisfy the *empty circumcircle interior property*, which states that all the circumcircles are empty, that is, there are no nodes inside any of the computed circumcircles.

[1] One of the scarce resources is the web page created by Marco Azzaro at http://www.ing.iac.es/~meteodat/blanks.htm, where a list of 38 blank fields are available.

2.2 Applying the Delaunay triangulation to the celestial sphere

Fortunately, the Delaunay triangulation is not restricted to the Euclidean two-dimensional case. It can be applied to other surfaces, in particular to the two-dimensional surface of a three-dimensional sphere. In this situation, the tessellation of the spherical surface is built on spherical triangles, that is, triangles on the sphere whose sides are great circles.

The empty circumcircle interior property of the Delaunay triangulation provides a straightforward method for a systematic search of regions in the celestial sphere free from stars. If one computes the Delaunay triangulation in the two-dimensional surface of a sphere, using as nodes locations of the stars down to a given threshold visual magnitude (m), then the above property guarantees that all the circumcircles are void of stars brighter than that magnitude (see Fig. 1). Thus, the circumdiameter of every circumcircle determines the maximum field of view that can be employed in that region of the sky as blank field.

In this work, we have applied the Delaunay triangulation to the Tycho-2 stellar catalogue. Tycho-2 contains astrometric and photometric information for the 2.5 million brightest stars in the sky, and it is complete up to magnitude $V = 11.5$ mag. Photometric data consist of two passbands ($B_{\rm T}$ and $V_{\rm T}$, close to Johnson B and V; Perryman et al. 1997). Typical uncertainties are 60 mas in position and 0.1 mag in photometry. In addition to the main catalogue, we have used the first Tycho-2 supplement, which lists another 17 588 bright stars from the *Hipparcos* and Tycho-1 catalogues which are not in Tycho-2.

In order to proceed with the triangulation, we have made use of STRIPACK (Renka 1997), a FORTRAN 77 software package that employs an incremental algorithm to build a Delaunay triangulation of a set of points on the surface of the unit sphere. For N nodes, the storage requirement for the triangulation is $13N$ integer storage locations in addition to $3N$ nodal coordinates. The computation scales as $O(N \log N)$. It is important to highlight that the original software was written using single-precision floating arithmetic, which turns out to be insufficient when dealing with astronomical coordinates with accuracy $\sim$1 arcsec. For the work presented here, we have modified the software code in order to use double-precision floating arithmetic, which guarantees proper computation of the triangulation when working with star separations approaching a few arcseconds.

2.2.1 Tessellating a collection of smaller subregions

In principle, it is straightforward to obtain a list of blank fields for the whole celestial sphere by using as input a stellar catalogue including stars down to a given magnitude. However, considering that the number of stars grows very rapidly with increasing limiting magnitude, this approach may turn out to become non-viable, either in terms of computer memory or considering computing time. In Fig. 2, we show the time taken by our computer in function of the number of stars (nodes) to carry out the tessellation of the Tycho-2 catalogue. Each dot corresponds to an increase of 0.5 mag in $m_{V_{\rm T}}$, in the range from 6.0 to 10.0 mag. Although the CPU time depends on the characteristic of the machine used for the tessellation, the most important aspect is the exponential increase in the required time with $m_{V_{\rm T}}$, mainly due to the exponential growth of the number of stars (see Table 1). In addition, since the tessellation of the whole celestial sphere demands memory storage (for stellar coordinates plus auxiliary variables) that scales with the number of stars,

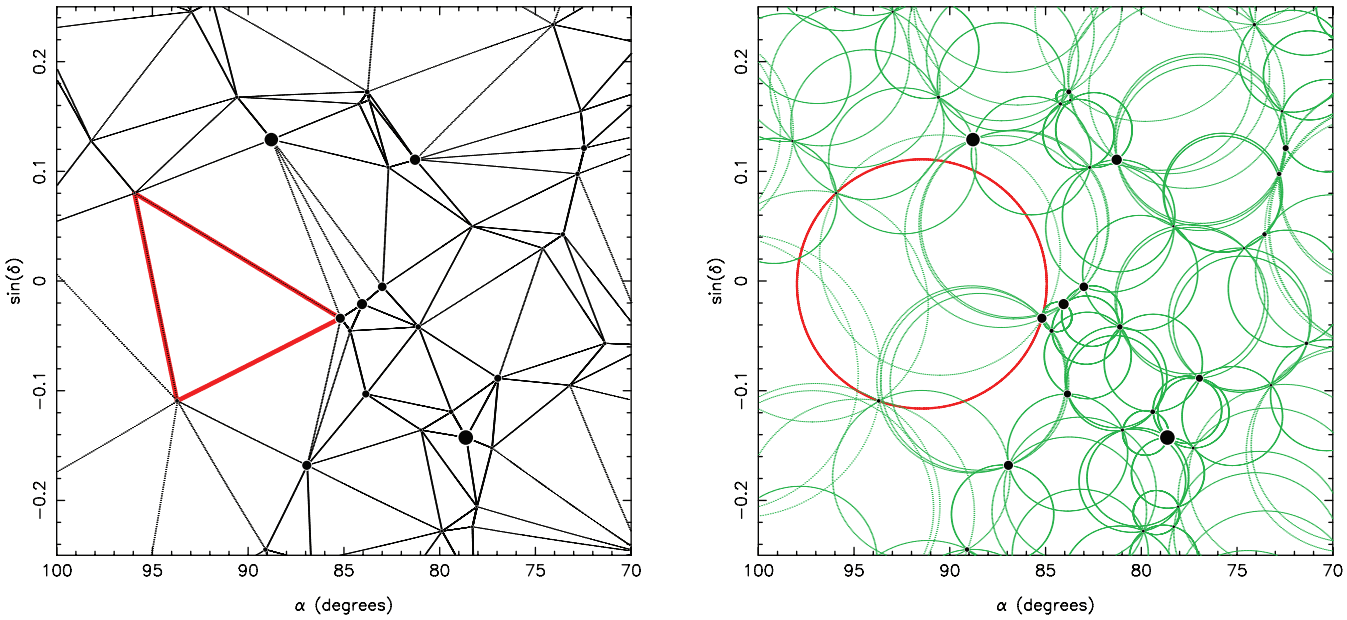

Figure 1. Application of the Delaunay triangulation to the celestial sphere. Left-hand panel: sky region centred at the Orion constellation ($\alpha = 5^{\rm h}40^{\rm m}$ and $\delta = 0^\circ$, J2000.0), represented using a Lambert's equal-area projection. All the stars brighter than $m_V = 4.5$ mag have been considered. Although each star is represented with a filled circle of size proportional to its brightness, the triangulation is carried out considering all the stars as nodes for the triangles, independently of their magnitude. A particular triangle is highlighted in red colour. Right-hand panel: circumcircles corresponding to all the triangles derived in the previous triangulation. The red circle indicates the circumcircle associated to the previously highlighted triangle. Note that the empty circumcircle interior property guarantees that there are no stars inside any of the displayed circumcircles.

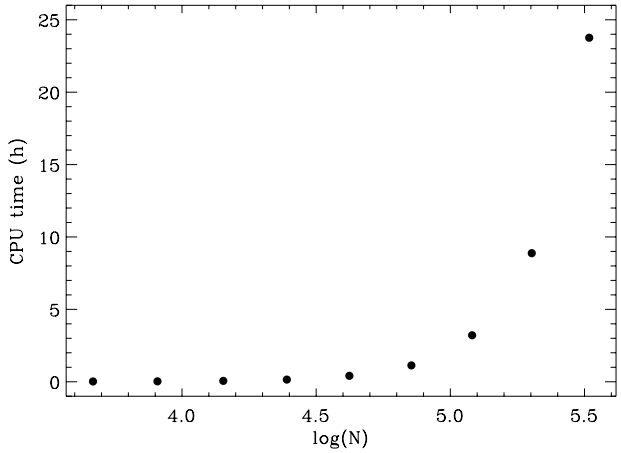

Figure 2. CPU time consumed in function of the number of stars (nodes) used in the tessellation. Each point corresponds to an increasing $m_{V_{\rm T}}$ from 6 to 10 in steps of 0.5 mag.

this approach requires excessively large memory capacity for faint magnitudes.

In these circumstances, our approach is to subdivide the whole celestial sphere into many smaller subregions (with some overlap among them), in order to individually compute the Delaunay triangulation in each of these smaller patches and, finally, merge the separate blank-field lists. However, the merging process is not immediate, since in this scenario the fact that the triangulation is computed in small subregions has an additional side-effect that must be properly handled: when the subregion area is smaller than a single hemisphere, the convex envelope of the stars within that subregion has an interior zone (the subregion) and a larger exterior zone (the celestial sphere excluding the considered subregion). This means that the triangulation has boundary edges, that is, triangle sides that are not shared with other triangles (see details in Renka 1997). In practice, the problem arises when one computes the circumcircles of the boundary triangles, since in these cases those circumcircles may easily expand beyond the limits of the considered subregion, where no stars are present because they have not been included as input for the triangulation. A graphical illustration of this problem is shown in Fig. 3.

Fig. 3(a) displays the initial triangulation obtained after computing the Delaunay triangulation of the subregion of the celestial sphere centred around the equatorial coordinates $\alpha = 6^{\rm h}$ and $\delta = 0^\circ$ (J2000.0) within a radius of 30°, and using stars brighter than $m_V = 4.5$ mag (note that the Orion constellation is close to the centre of the field, whereas the bright stars Sirius, Procyon and Aldebaran appear towards the south-east, east and north-west, respectively). The sky region is represented using a Lambert's equal-area projection (Calabretta & Greisen 2002). The thick red line indicates the limit of the 30° radius. Once the triangulation has been computed, the next step is the calculation of the circumcircle associated to each triangle. Fig. 3(b) shows all the circumcircles obtained for the triangulation derived in the previous step. The circumcircles that are fully circumscribed within the 30° radius are displayed with green colour, whereas the circumcircles that expand beyond that limit are represented in magenta. It is obvious that the latter will not be, in general, appropriate blank fields, since they have been computed assuming that no stars were present beyond the red thick line. However, even in these cases, several possibilities can be envisaged in order to obtain valid blank fields starting from the information provided by the affected boundary triangles, while respecting the constraint imposed by the proximity of the boundary of the subregion. We discuss in Appendix A several of these possibilities. The result of following such approach is shown in Fig. 3(c).

Table 1. Results of the tessellation process using the Tycho-2 catalogue with the V_T filter. Down to $m_{V_T} = 10$ mag, the Delaunay triangulation has been obtained using the resulting stellar catalogues corresponding to the whole celestial sphere. For $m_{V_T} = 10.5$ and 11.0, the results correspond to combining the individual triangulation of smaller sky subregions, as explained in the text (see Section 2.2.1). The last five rows of this table indicate the coefficients corresponding to the linear regressions $y = a + bx$, where $x = m_{V_T}$ in all the cases and y has been set to the logarithm (with base 10) of the considered parameters where the linear fit makes sense. See description of the different columns in Section 2.3.

(1) m_{V_T} (mag)	(2) N_*	(3) N_{BF}	(4) ρ_{median} (°)	(5) Δh (°)	(6) A	(7) $\overline{\rho}$ (°)	(8) σ_ρ (°)	(9) ρ_{max} (°)	(10) B	(11) f	(12) ν	(13) CPU time (h)
6.0	4648	9,292	2.111	0.120	4.796×10^2	2.067	0.928	5.805	4.879×10^2	0.436	10	0.02
6.5	8083	16 162	1.592	0.110	1.026×10^3	1.559	0.691	5.047	1.033×10^3	0.581	11	0.03
7.0	14 229	28 454	1.211	0.080	1.730×10^3	1.182	0.525	3.702	1.747×10^3	0.767	11	0.06
7.5	24 551	49 098	0.914	0.060	2.938×10^3	0.893	0.400	2.932	2.981×10^3	1.011	10	0.15
8.0	41 989	83 974	0.696	0.052	5.776×10^3	0.679	0.302	2.510	5.830×10^3	1.335	11	0.41
8.5	71 491	142 978	0.528	0.042	1.030×10^4	0.514	0.233	2.051	1.052×10^4	1.752	10	1.13
9.0	120 381	240 758	0.405	0.032	1.707×10^4	0.392	0.180	1.557	1.767×10^4	2.294	10	3.21
9.5	200 835	401 666	0.310	0.026	2.988×10^4	0.300	0.140	1.273	3.128×10^4	2.995	10	8.88
10.0	328 819	657 634	0.240	0.022	5.291×10^4	0.231	0.109	1.051	5.570×10^4	3.850	9	23.76
10.5	538 719	1077 434	0.185	0.020	1.005×10^5	0.177	0.086	0.943	1.077×10^5	4.998	9	–
11.0	871 336	1742 668	0.143	0.018	1.850×10^5	0.137	0.068	0.853	2.026×10^5	6.460	9	–
a	0.96	1.27	1.719	–	−0.31	1.725	1.31	1.80	−0.35	−1.753	–	−6.7
Δa	0.03	0.03	0.011	–	0.04	0.009	0.02	0.05	0.04	0.012	–	0.2
b	0.455	0.455	−0.2339	–	0.506	−0.2362	−0.227	−0.176	0.513	0.2340	–	0.80
Δb	0.004	0.004	0.0013	–	0.004	0.0011	0.002	0.006	0.005	0.0014	–	0.03
r^2	0.9994	0.9994	0.9997	–	0.9992	0.9998	0.9990	0.9901	0.9993	0.9997	–	0.9909

Finally, the blank-field lists obtained for the different sky subregions need to be merged. In our case, we have applied this procedure when tessellating the sky for $m_{V_T} = 10.5$ and 11.0 mag. In particular, we have divided the whole celestial sphere into 578 circular subregions of 8° radius, where the centre of each subregion is separated by 6° in declination and by $6°/\cos\delta$ in right ascension. Considering that the maximum blank-field radius obtained for $m_{V_T} = 10.0$ mag is ∼1° (see Table 1), this separation between subregions provides an excellent overlap between them. Within the overlapping areas, there are duplicated blank fields and additional blank fields that were not permitted to expand beyond their corresponding boundary limit. Consequently, to obtain the final catalogue, we have removed both the repeated blank fields and those due to the border effect (typically inscribed within larger blank fields of neighbouring subregions). The latter were easy to identify because they circumscribe less than three stars. Thus, the final all-sky blank-field catalogue is not affected by the number, size and overlap of the subregions that we have employed.

2.2.2 Preparing the nodes for the triangulation

As described above, Tycho-2 provides photometry data in two passbands (B_T and V_T). We have applied the Delaunay triangulation to each passband separately and to the combination of both. To obtain the initial collection of stars, we have selected from both the main and the supplement Tycho-2 catalogues all stars with magnitude lower than m in a given filter. In the case of using both filters, the star magnitude should be lower than m in either of the two filters.

These initial collections of stars are still not suitable to compute the Delaunay triangulation due to the presence of stars with insufficient separation. For that reason, we decided to 'merge' into single objects all the stars closer than 1 arcsec, similar to a typical seeing under good weather conditions. The resulting visual magnitude for the combined objects was computed as the sum of the fluxes of the merged stars. The coordinates of the new objects were placed in the line connecting the merged stars, closer to the brightest star (using a weighting scheme dependent on the individual brightness of the combined stars). This merging process does not reduce substantially the final number of stars, but it makes the triangulation process easier by removing unnecessary very small triangles for which the computations are prone to rounding errors.

2.3 Results

We have applied the triangulation method to the merged star lists as described above, with threshold magnitudes between 6 and 11 mag in steps of 0.5 mag. The resulting blank-field catalogues are accessible through the TESELA tool (explained in Section 3).

As an example, we present the results of the triangulation for V_T in Fig. 4. The different histograms correspond to the distributions of the number of blank fields as a function of blank-field radius, for different threshold magnitudes m_{V_T}. The resulting histograms are positively skewed and although, as a first-order approach, they can approximately be fitted with a normal distribution (green curves), better fits are obtained using χ^2_ν functions with ν degrees of freedom (red curves). Note that the use of a chi-square law is just an empirical result, obtained after trying to fit different well-known skewed distributions, like lognormal and F_{ν_1,ν_2} distributions (the latter with ν_1 and ν_2 degrees of freedom), and finding that the best fits were obtained using F_{ν_1,ν_2} when $\nu_2 \to \infty$, which is equivalent to using a $\chi^2_{\nu_1}$ distribution (see e.g. Press et al. 2007). It is not the goal of this work to provide a physical justification for this behaviour.

The quantitative description of the above results is presented in Table 1. The threshold magnitude m_{V_T} is given in the first column. The number of stars N_* (i.e. nodes) and the number of blank-field regions found, N_{BF}, are listed in the second and third columns, respectively. Column (4) indicates the median blank-field

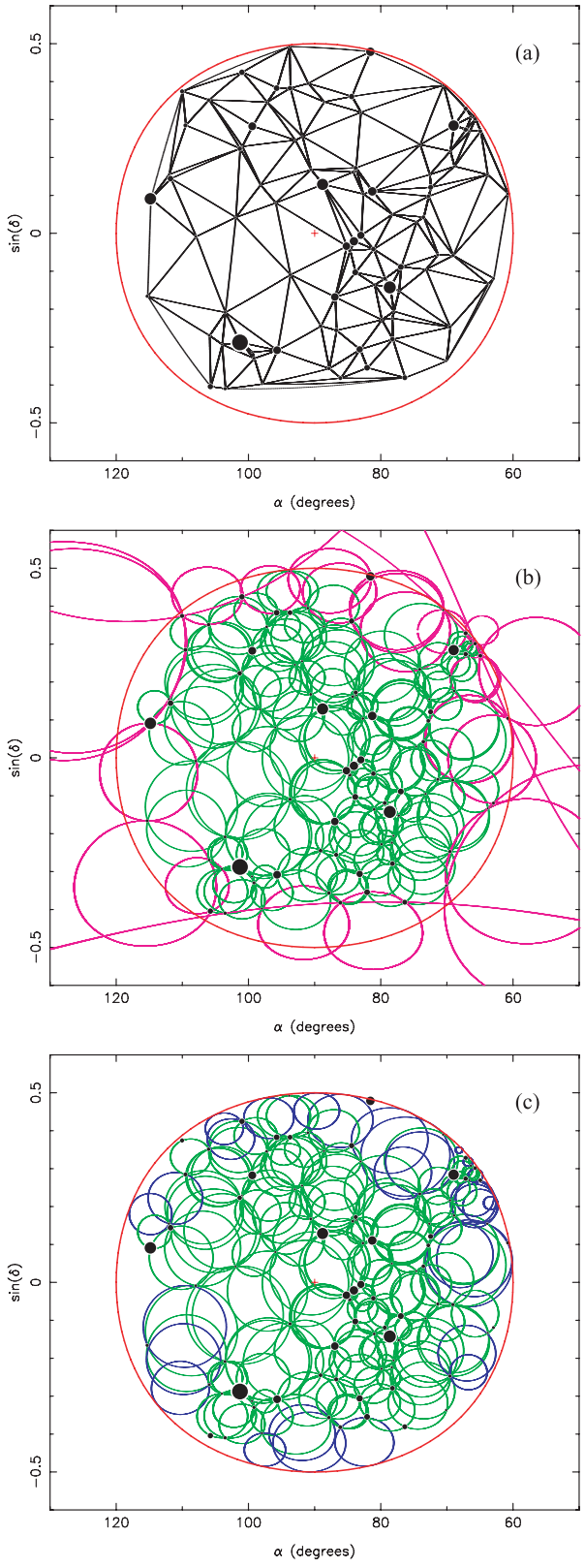

Figure 3. Graphical illustration of the tessellation procedure when handling a subregion of the sky, in particular the portion of the celestial sphere (here represented using a Lambert's equal-area projection) centred around the equatorial coordinates $\alpha = 6^{\rm h}$ and $\delta = 0^\circ$ (J2000.0) within a radius of 30°, and using stars brighter than $m_V = 4.5$ mag. See explanation in the text (Section 2.2.1).

radius $\rho_{\rm median}$ and column (5) indicates the bin width Δh for the histogram distributions (some of them displayed in Fig. 4) employed to derive the parametric fits given in the subsequent columns. The amplitude A, mean radius $\overline{\rho}$ and standard deviation σ_ρ, obtained from the fit of each histogram to a normal distribution of the form $A\exp[-(\rho-\overline{\rho})^2/(2\sigma_\rho^2)]$, are listed in columns (6), (7) and (8), respectively. The maximum blank-field radius appears in column (9). The coefficients of the fit to a chi-square distribution of the form $B\,\chi^2_\nu(\rho/f)$, where B is the amplitude, f is a scaling factor for ρ and ν is the number of degrees of freedom, are given in columns (10)–(12). Finally, column (13) indicates the CPU time taken for the triangulation when tessellating the whole celestial sphere at once.

As shown in Fig. 2, the required CPU computing time increases exponentially with m. For this reason, we have derived the Delanuay triangulation for the whole celestial sphere at once just up to magnitude 10, and in overlaping smaller regions (as explained in Section 2.2.1) for higher m.

2.4 Analysis

We have analysed the results of the triangulation for $V_{\rm T}$. For $B_{\rm T}$ and the combination of both filters, the results are very similar.

Not surprisingly, there is an excellent correlation between most of the parameters listed in Table 1 and $m_{V_{\rm T}}$. The correlations can be very well fitted using linear regressions of the form $y = a + bx$, being $x = m_{V_{\rm T}}$, and defining y as the base-10 logarithm of the considered parameter. The intercept a and slope b of the regressions (together with their associated uncertainties Δa and Δb) are given at the bottom of each column. The final entry indicates the coefficient of determination, r^2, which in all the cases reveals the excellent correlation between the fitted data.

It is also interesting to examine the characteristics of the derived blank fields at a given limiting magnitude. For example, we have analysed two illustrative diagrams corresponding to the case $m_{V_{\rm T}} = 11.0$, which are represented in Fig. 5. Fig. 5(a) displays the variation in the number of regions as a function of the absolute value of Galactic latitude l. Not surprisingly, the number of regions must decrease as the latitude increases, since the area of a spherical annulus (shown with the red symbols) is maximum at the Galactic equator and tends to zero when $|l|$ approaches 90°. However, this variation is not enough to explain the difference between the histogram and the red symbols, which clearly indicates that the number of regions is highly concentrated towards the Galactic equator, which is simply the result of the higher stellar density in that region. Fig. 5(b) shows that even though the number of available blank fields unavoidably decreases with Galactic latitude, their typical size, and the variation in sizes between them, increases with l approaching the Galactic poles.

The extrapolation to fainter magnitudes of the exponential variations of the parameters listed in Table 1, together with the unavoidable increasing difficulty when approaching low Galactic latitudes, strongly supports the need for an automatic tool that helps to identify suitable blank fields when observing with medium-/large-size telescopes.

3 TESELA

In order to provide an easy way to access the blank-field catalogues, we have created TESELA, a tool accessible through the Internet,

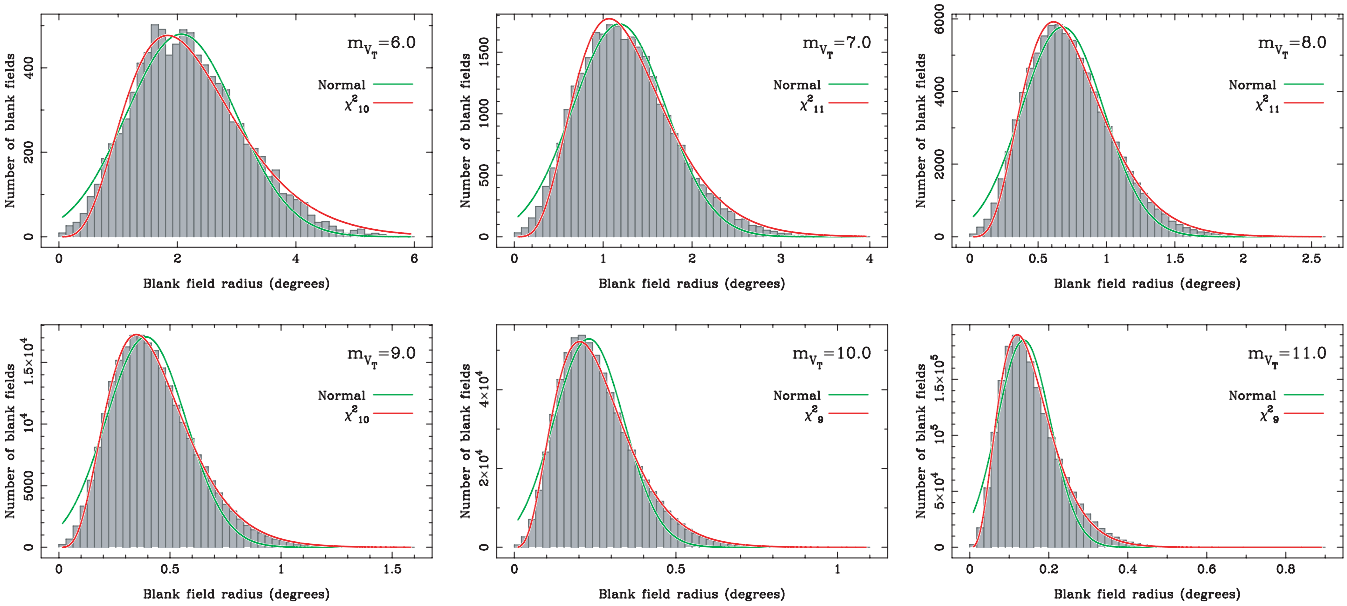

Figure 4. Histograms with the distributions of blank-field radius, for different values of m_{V_T}, as indicated in the upper right-hand inset of each diagram. Note that the x-axis range decreases as m_{V_T} increases. The green curve is the fit to a normal distribution, whereas the red line indicates the corresponding fit to a χ^2_ν distribution with ν degrees of freedom. The coefficients of these parametric fits are given in Table 1. The best fit in all the diagrams is obtained for the χ^2_ν distribution.

developed under the Spanish Virtual Observatory project,[2] which is publicly available at the following URL:

http://sdc.cab.inta-csic.es/tesela.

The tool consists of a data base containing the Tycho-2 stars and the already computed blank-field regions, and an user-friendly interface for accessing the data. TESELA allows the users to perform a cone-search around a position in the sky, that is, to obtain the list of blank fields available around a given sky position (right ascension and declination) and within a fixed radius around that position. Through its search form (see Fig. 6), users can select the threshold magnitude m, the Tycho-2 filter to be used (B_T, V_T or the combination of both) and define a minimum radius for the blank-field regions. This last option may be especially important to fulfil observing requirements, for example, to ensure that the blank field is larger than the field of view of a given instrument.

TESELA presents the result of the cone-search in two tables, one for blank fields (RA, Dec., radius) and the other for the Tycho-2 stars (RA, Dec., m_{B_T} and/or m_{V_T}) in the searching area. These tables can be downloaded in CSV format for further use. TESELA also provides users with the possibility of visualizing the data. To do that, TESELA takes advantage of ALADIN[3] Bonnarel et al. (2000), a Virtual Observatory (VO) compliant software that allows users to visualize and analyse digitized astronomical images, and superimpose entries from astronomical catalogues or data bases available from the VO services. Thanks to this connection with ALADIN, we have provided TESELA with the full capacity and power of the VO.

In Fig. 7, we show an example of how TESELA visualizes the data using ALADIN. TESELA sends to ALADIN the Tycho-2 stars of the region, which are loaded in the first plane. The search area is plotted in a second layer with a red circle; another layer depicting the blank fields with blue circles is created and, finally, a last layer shows the objects of NGC 2000.0 (the complete new general catalogue and

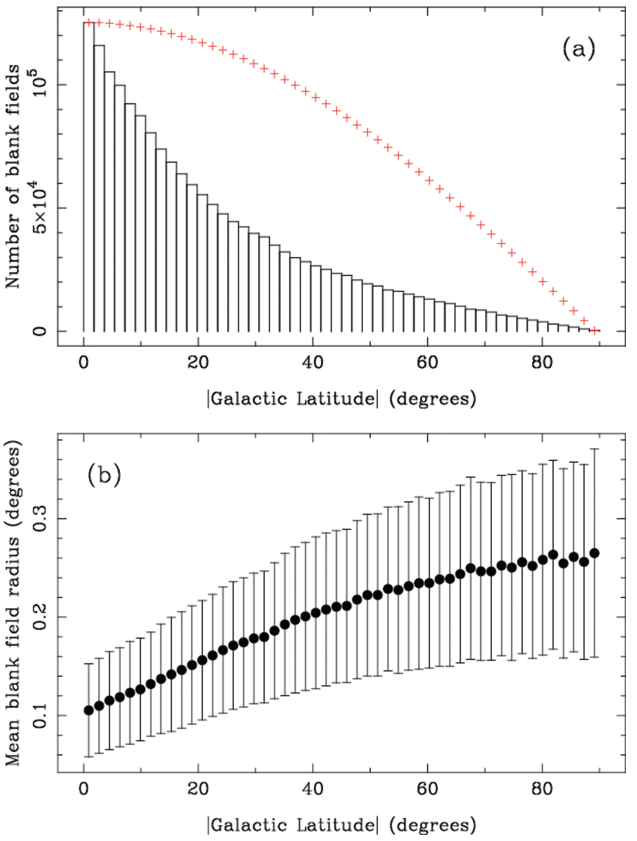

Figure 5. Properties of the blank fields obtained in the case $m_{V_T} = 11.0$ mag. Diagram (a): number of blank fields as a function of the absolute value of the Galactic latitude. The red symbols show the relative variation of the surface area on the celestial sphere with Galactic latitude. Diagram (b): variation of the mean circumcircle radius as a function of the absolute value of the Galactic latitude (the error bars indicate the rms exhibited by the radii at each Galactic latitude bin).

[2] http://svo.cab.inta-csic.es/
[3] http://aladin.u-strasbg.fr/

Figure 6. TESELA's search form. Through it the user defines the value of several parameters used for the cone-search. This form is available at http://sdc.cab.inta-csic.es/tesela.

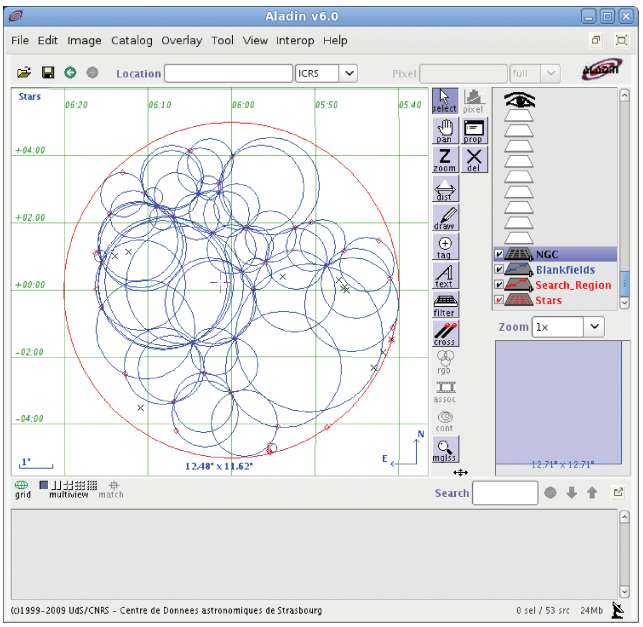

Figure 7. Example of visualization of the data with ALADIN. The large red circle defines the searching area, Tycho-2 stars are shown by the red diamonds, the blue circles depict the blank fields and the black sails are the objects of NGC 2000.0 in the region.

index catalogue of nebulae and star clusters, Sinnott 1997). Using this ALADIN window, users are allowed to load images and catalogues both locally and from the VO, having full access to the whole universe resident in the VO. This can be very helpful to determine the potential influence of relatively bright nebulae and extragalactic sources in the sought regions. Note also that, for obvious reasons, Solar system objects have been not considered, and they must be taken into account in order to make use of blank-field regions close to the ecliptic at a given date.

So far, the current version of TESELA allows users to access a collection of blank fields obtained from the optical Tycho-2 catalogue. However, TESELA has been conceived as a dynamic tool, which will be improved in the future with both deeper optical catalogues and catalogues in others wavelength ranges. Any future change in the tool will be properly documented in its website.

ACKNOWLEDGMENTS

We would like to thank the anonymous referee for the careful reading of the manuscript and for her/his comments, which have helped to clarify this paper. This work was partially funded by the Spanish MICINN under the Consolider-Ingenio 2010 Program grant CSD2006-00070: First Science with the GTC.[4] This work was also supported by the Spanish Programa Nacional de Astronomía y Astrofísica under grants AYA2008-02156 and AYA2009-10368, and by AstroMadrid[5] under project CAM S2009/ESP-1496. This work has made use of ALADIN developed at the Centre de Données Astronomiques de Strasbourg, France.

REFERENCES

Bonnarel F., Fernique P., Bienaymé O. et al., 2000, A&AS, 143, 33
Calabretta M. R., Greisen E. W., 2002, A&A, 395, 1077
Delaunay B., 1934, Sur la sphère vide, Bull. Acad. Sci. USSR, 793, 7
Gilliland R. L., 1992, in Howell S. B., ed., ASP Conf. Ser. Vol. 23, Astronomical CCD Observing and Reduction Techniques. Astron. Soc. Pac., San Francisco, p. 68
Høg E., Fabricius C., Makarov V. V. et al., 2000, A&A, 355, L27
Perryman M. A. C., Lindegren L., Kovalevsky J. et al., 1997, A&A, 323, L49
Press W. H., Teukolsky S. A., Vetterling W. T., Flannery B. T., 2007, Numerical Recipes: The Art of Scientific Computing, 3rd edn. Cambridge Univ. Press, New York
Renka R. J., 1997, ACM Trans. Math. Softw., 23, 416
Sinnott R. W., 1997, VizieR Online Data Catalog, VII/118, 0
Weisstein E. W., 2011, Sphere Point Picking. From MathWorld – A Wolfram Web Resource: http://mathworld.wolfram.com/SpherePointPicking.html

APPENDIX A: HANDLING BOUNDARY TRIANGLES

Although tessellating small sky subregions is a good approach to solving the problem of deriving blank fields when dealing with very large stellar catalogues, the discussion in Section 2.2.1 revealed that the Delaunay triangulation of such subregions leads to the situation displayed in Fig. 3(b), where many circumcircles associated with boundary triangles (shown in magenta colour in that figure) clearly expand beyond the limit of the considered subregion. Although in this case those circumcircles can be easily discarded, it is possible to derive, starting from the coordinates of the corresponding boundary triangles, new circles devoided of stars that remain within the boundary of the sky subregion. This appendix describes in more detail different approaches that can be employed in this circumstance.

In what follows, we consider the celestial sphere as the unit sphere centred at the origin $\boldsymbol{O}$. The sky subregion where the blank

[4] http://www.iac.es/consolider-ingenio-gtc
[5] http://www.astromadrid.es

fields will be searched for is the surface of a spherical cap, which centre is given by the unit vector $\boldsymbol{K}_{\rm sky}$, and the angular radius of such subregions, as measured from $\boldsymbol{O}$, is $\theta_{\rm max}$ (see Fig. A1). The Delaunay triangulation will be computed with all the stars (down to a given magnitude) within that sky subregion. Denoting the unit vectors pointing to these stars as $\boldsymbol{S}_i$ (with $i = 1, \ldots, N_{\rm stars}$, $N_{\rm stars}$ being the total number of stars within the subregion), it is obvious that the condition that all these stars must satisfy is

$$\theta_{\rm max} \geq \arccos(\boldsymbol{K}_{\rm sky} \cdot \boldsymbol{S}_i), \ \forall i = 1, \ldots, N_{\rm stars}. \quad \text{(A1)}$$

We also assume that $\theta_{\rm max} < \pi/2$, that is, the sky subregion area under consideration is smaller than a single hemisphere.

Discovering problematic boundary circumcircles

The Delaunay triangulation provides the coordinates of the three nodes (stars) of all the triangles resulting from the tessellation procedure (see Fig. A1). Let us denote the unit vectors pointing from $\boldsymbol{O}$ towards the three nodes of each triangle, given in counterclockwise order, as $\boldsymbol{Q}_1$, $\boldsymbol{Q}_2$ and $\boldsymbol{Q}_3$. The unit vector $\boldsymbol{C}$ marking the circumcentre of any triangle can be easily computed as (see e.g. Renka 1997)

$$\boldsymbol{C} = \frac{(\boldsymbol{Q}_2 - \boldsymbol{Q}_1) \times (\boldsymbol{Q}_3 - \boldsymbol{Q}_1)}{||(\boldsymbol{Q}_2 - \boldsymbol{Q}_1) \times (\boldsymbol{Q}_3 - \boldsymbol{Q}_1)||}. \quad \text{(A2)}$$

Note that since the three nodes define a plane, the two vectors $(\boldsymbol{Q}_2 - \boldsymbol{Q}_1)$ and $(\boldsymbol{Q}_3 - \boldsymbol{Q}_1)$ are contained in that plane, and their cross-product provides a new vector perpendicular to the plane. Of the two possible directions of that vector, the fact that the nodes are given in counterclockwise order guarantees that $\boldsymbol{C}$ points towards the spherical triangle defined by $\boldsymbol{Q}_1$, $\boldsymbol{Q}_2$ and $\boldsymbol{Q}_3$. In addition, the modulus calculated in the denominator of equation (A2) assures that $\boldsymbol{C}$ is normalized. It is not difficult to show that the circumcentre is equidistant from all the three nodes, which allows us to compute the circumradius of the circumcircle from the inner product of $\boldsymbol{C}$ with any of the node vectors,

$$r_C = \arccos(\boldsymbol{C} \cdot \boldsymbol{Q}_i), \qquad \text{with } i = 1, 2 \text{ or } 3. \quad \text{(A3)}$$

On the other hand, the angular distance between the circumcentre and the centre of the sky subregion can be determined as

$$d_C = \arccos(\boldsymbol{C} \cdot \boldsymbol{K}_{\rm sky}).$$

The condition that must be met for any circumcircle to be inscribed within that subregion is then

$$d_C + r_C \leq \theta_{\rm max}. \quad \text{(A4)}$$

If the above condition does not hold, the computed circumcircle expands beyond the sky subregion and cannot be used as a valid blank field. Under this circumstance, other options need to be considered, as explained in the following steps.

Step 0: compute the circle inscribed in the triangle

No matter how close to the boundary of the sky subregion is located any triangle computed during the tessellation, the circle inscribed in those triangles are always within the subregion. These *incircles* are centred at a particular point, the *incentre*, which is equidistant from the three sides of the triangles and corresponds to the intersection of the three bisectors through the vertices of those triangles (see Fig. A2a). The unit vector $\boldsymbol{I}$ pointing from $\boldsymbol{O}$ towards the incentre

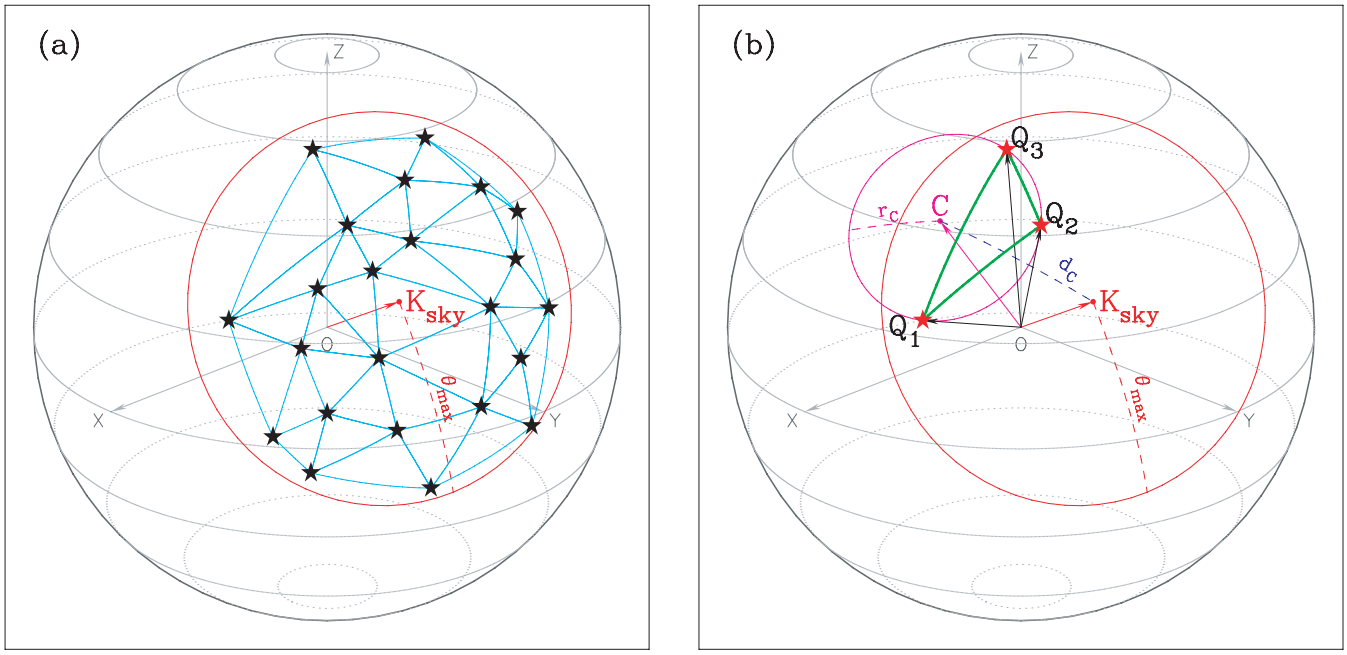

Figure A1. Graphical illustration of the notation employed in Appendix A to explain the initial steps when handling boundary triangles. Diagram (a): the whole celestial sphere of unit radius and centred at the origin $\boldsymbol{O}$ is displayed in grey. The sky subregion under tessellation, which boundary is shown in red, is centred at the point indicated by the unit vector $\boldsymbol{K}_{\rm sky}$ and has a radius $\theta_{\rm max}$ (dashed red line) measured along a great circle on the surface of the celestial sphere. Only the stars contained within this region are employed to compute the Delaunay triangulation (shown in cyan). Diagram (b): a sample boundary triangle formed by the stars located at $\boldsymbol{Q}_1$, $\boldsymbol{Q}_2$ and $\boldsymbol{Q}_3$, given in counterclockwise order, is represented in green. Its corresponding circumcircle, centred at $\boldsymbol{C}$ and passing through the three node stars, is displayed in magenta. The radius of this circumcircle r_C is plotted with a dashed magenta line. The angular distance d_C between $\boldsymbol{C}$ and $\boldsymbol{K}_{\rm sky}$ is shown with a dashed blue line. In this example, the circumcircle expands beyond the limit of the sky subregion, that is, the condition given in equation (A4) does not hold.

of a given triangle can be obtained as

$$\boldsymbol{I} = \frac{(\boldsymbol{N}_{1,2} - \boldsymbol{N}_{3,1}) \times (\boldsymbol{N}_{2,3} - \boldsymbol{N}_{1,2})}{||(\boldsymbol{N}_{1,2} - \boldsymbol{N}_{3,1}) \times (\boldsymbol{N}_{2,3} - \boldsymbol{N}_{1,2})||}, \tag{A5}$$

where $\boldsymbol{N}_{i,j}$ is the unitary vector perpendicular to the plane defined by the origin and the nodes at $\boldsymbol{Q}_i$ and $\boldsymbol{Q}_j$,

$$\boldsymbol{N}_{i,j} = \frac{\boldsymbol{Q}_i \times \boldsymbol{Q}_j}{||\boldsymbol{Q}_i \times \boldsymbol{Q}_j||}. \tag{A6}$$

Defined in this way, and considering that the three triangle nodes are given in counterclockwise order, the three normal vectors $\boldsymbol{N}_{1,2}$, $\boldsymbol{N}_{2,3}$ and $\boldsymbol{N}_{3,1}$ are always pointing towards the interior of the triangles. It is also easy to show that the inner product $\boldsymbol{I} \cdot \boldsymbol{N}_{i,j}$ provides the radius of the incircle as

$$r_I = \arcsin(\boldsymbol{I} \cdot \boldsymbol{N}_{i,j}), \tag{A7}$$

whose value is the same for $(i, j) = (1, 2)$, $(2, 3)$ or $(3, 1)$. Note the use of the arcsin function instead of the arccos function in the above expression; since $\boldsymbol{N}_{i,j}$ is perpendicular to the plane defined by the origin $\boldsymbol{O}$ and the nodes at $\boldsymbol{Q}_i$ and $\boldsymbol{Q}_j$, the angular distance r_I between $\boldsymbol{I}$ and that plane must be computed as $\pi/2$ minus the angle subtended by $\boldsymbol{I}$ and $\boldsymbol{N}_{i,j}$.

By construction, it is obvious that incircles will always be regions devoided of stars, since they are inscribed in the considered triangles, which, in turn, are inscribed in the circumcircles, which, by the empty circumcircle interior property (see Section 2.1), do not contain any star. For that reason they constitute a first solution to the problem with the boundary triangles which circumcircles expand beyond the limit of the sky subregion under tessellation.

Step 1: enlarge the radius towards the triangle nodes

Once the incircle of a given boundary triangle has been computed, it is very likely that the incentre does not coincide with the circumcentre. In this case, it is possible to enlarge the incircle by increasing the radius r_I to the closest triangle node as measured from the incentre (see Fig. A2b). To facilitate the explanation of the procedure,

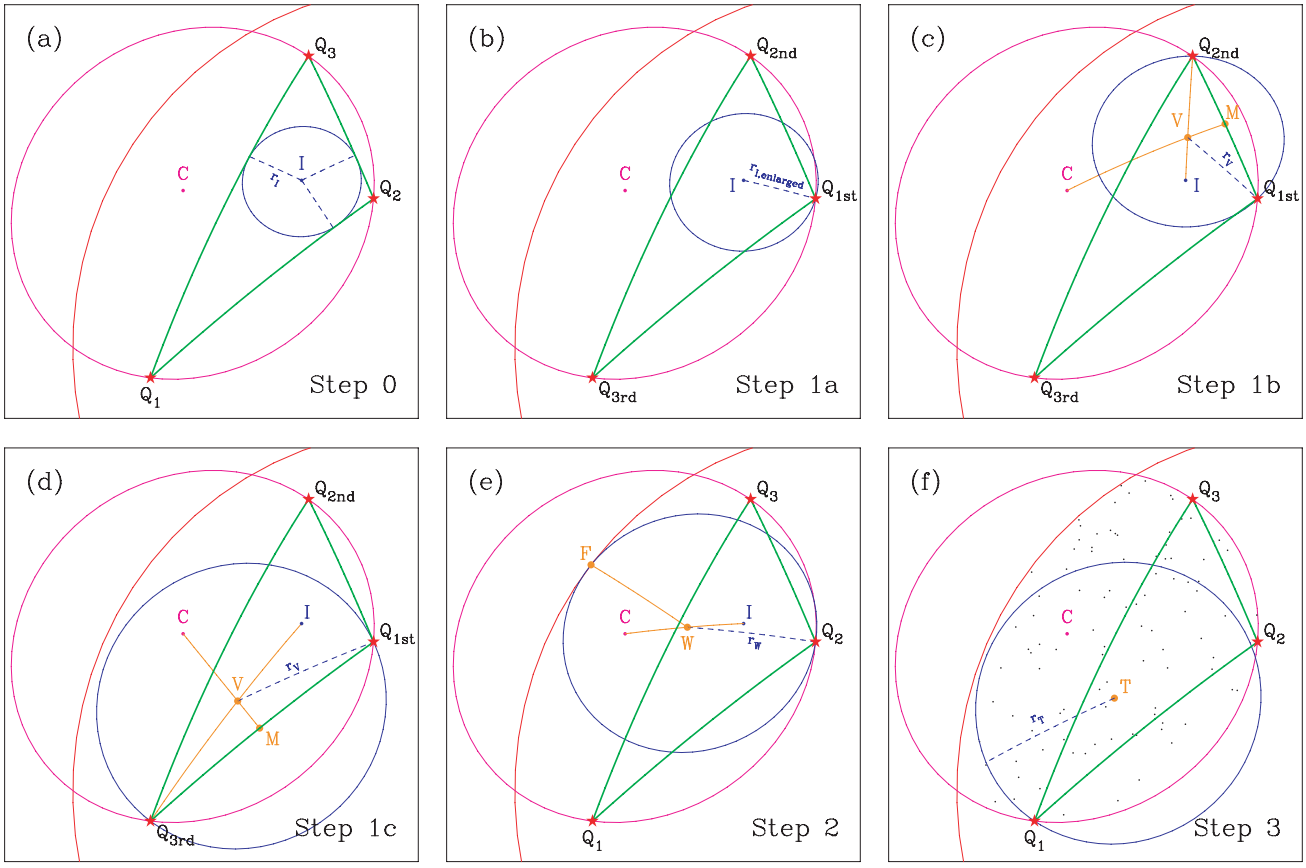

Figure A2. Different strategies described in Appendix A to obtain a valid blank field in the neighbourhood of a boundary triangle. These diagrams represent an enlargement of the example represented in Fig. A1, where, for clarity, some graphical elements represented in Fig. A1 have been removed. Diagram (a): computation of the incircle, the circle inscribed in the spherical triangle. It is centred at $\boldsymbol{I}$ and is displayed in blue. The distance from $\boldsymbol{I}$ to each of the sides of the boundary triangle is the same, r_I. Diagram (b): enlargement of the initial incircle until reaching the closest star in the boundary triangle. Note that the three stars at the vertices of the spherical triangle have been renamed as $\boldsymbol{Q}_{1st}$, $\boldsymbol{Q}_{2nd}$ and $\boldsymbol{Q}_{3rd}$ to indicate their order of proximity to the incentre. Thus, the resulting new radius, $r_{I,\mathrm{enlarged}}$, is the angular distance between the incircle $\boldsymbol{I}$ and $\boldsymbol{Q}_{1st}$. Diagram (c): displacement of the centre of the blank field along the great circle connecting the incentre $\boldsymbol{I}$ with the second nearest triangle node $\boldsymbol{Q}_{2nd}$. The new centre $\boldsymbol{V}$ is equidistant from the nodes $\boldsymbol{Q}_{1st}$ and $\boldsymbol{Q}_{2nd}$. Diagram (d): displacement of the centre of the blank field along the great circle connecting the incentre $\boldsymbol{I}$ with the farthest triangle node $\boldsymbol{Q}_{3rd}$. The new centre $\boldsymbol{V}$ is equidistant from the nodes $\boldsymbol{Q}_{1st}$ and $\boldsymbol{Q}_{3rd}$. Diagram (e): displacement of the centre of the blank field along the great circle connecting the incentre $\boldsymbol{I}$ and the circumcentre $\boldsymbol{C}$. The distance r_W between the new centre $\boldsymbol{W}$ and the nearest triangle star is the same as the distance from the boundary of the sky subregion, indicated by $\boldsymbol{F}$. Diagram (f): random search of a valid blank field around the spherical triangle defined by $\boldsymbol{Q}_1$, $\boldsymbol{Q}_2$ and $\boldsymbol{Q}_3$. The black dots are random points in the intersection of the circumcircle and the sky subregion. Each of these points is checked as the centre of a potential blank field. The blue circle, with centre $\boldsymbol{T}$ and radius r_T, indicates the largest of such circles that satisfy the conditions for a valid blank field.

let us rename the unit vectors pointing towards the three nodes of each triangle as $\boldsymbol{Q}_{1st}$, $\boldsymbol{Q}_{2nd}$ and $\boldsymbol{Q}_{3rd}$, where the subscript indicates the ordering of the nodes as a function of their proximity to the incentre.

The enlargement of the angular distance connecting $\boldsymbol{I}$ with $\boldsymbol{Q}_{1st}$ provides a new radius that can be expressed as

$$r_{\boldsymbol{I},\mathrm{enlarged}} = \arccos(\boldsymbol{I} \cdot \boldsymbol{Q}_{1st}). \quad \text{(A8)}$$

However, although the new enlarged circle will only pass through one of the nodes and leave outside the other two nodes, it is possible that other neighbouring stars can enter into its interior. For that reason, instead of equation (A8) it is necessary to use

$$r_{\boldsymbol{I},\mathrm{enlarged}} = \mathrm{minimum}\left[\arccos(\boldsymbol{I} \cdot \boldsymbol{S}_i)\right], \ \forall i = 1, \ldots, N_{\mathrm{stars}}, \quad \text{(A9)}$$

which already includes the relation given in equation (A8), since the three nodes are part of the set of stars.

Before accepting $r_{\boldsymbol{I},\mathrm{enlarged}}$ as a valid radius for a blank field, it is required to check that with this new radius the resulting circle (centred at the triangle incentre) does not exceed the boundary of the sky subregion. This is performed in a similar way to that previously employed in step 0. First, the angular distance between the incentre and the centre of the sky subregion is determined as

$$d_I = \arccos(\boldsymbol{I} \cdot \boldsymbol{K}_{\mathrm{sky}}).$$

The condition that must be met by the enlarged circle is then

$$d_I + r_{I,\mathrm{enlarged}} \leq \theta_{\mathrm{max}}. \quad \text{(A10)}$$

If the above condition is not satisfied, a revised version of the radius can be computed as

$$r_{I,\mathrm{enlarged,revised}} = \theta_{\mathrm{max}} - d_I. \quad \text{(A11)}$$

Note that, so far, the valid blank field is still centred around the triangle incentre. However, by removing this constraint, it is possible to obtain an even larger valid blank field by allowing its centre to move from the incentre towards the directions of the other two nodes following the great circles connecting these points.

Next, we describe the procedure of shifting the centre of the blank field along the line connecting the incentre with the node corresponding to $\boldsymbol{Q}_{2nd}$. The resulting new centre $\boldsymbol{V}$ (see Fig. A2c) will be a point equidistant from $\boldsymbol{Q}_{1st}$ and $\boldsymbol{Q}_{2nd}$. The situation with the third node can be obtained by substituting $\boldsymbol{Q}_{2nd}$ with $\boldsymbol{Q}_{3rd}$ in the following description (see Fig. A2d).

The first step consists in computing the mid-point in the triangle side connecting $\boldsymbol{Q}_{1st}$ and $\boldsymbol{Q}_{2nd}$. The unitary vector pointing towards this point is given by

$$\boldsymbol{M} = \frac{\boldsymbol{Q}_{1st} + \boldsymbol{Q}_{2nd}}{||\boldsymbol{Q}_{1st} + \boldsymbol{Q}_{2nd}||}. \quad \text{(A12)}$$

The sought new centre $\boldsymbol{V}$ can be obtained as the intersection of the great circle defined by the two vectors $\boldsymbol{M}$ and $\boldsymbol{C}$ with the great circle defined by the two vectors $\boldsymbol{I}$ and $\boldsymbol{Q}_{2nd}$. This intersection can be easily computed as

$$\boldsymbol{V} = \pm\frac{(\boldsymbol{C} \times \boldsymbol{M}) \times (\boldsymbol{I} \times \boldsymbol{Q}_{2nd})}{||(\boldsymbol{C} \times \boldsymbol{M}) \times (\boldsymbol{I} \times \boldsymbol{Q}_{2nd})||}, \quad \text{(A13)}$$

where the $\pm$ sign indicates two initial solutions from which the closest vector to $\boldsymbol{I}$ must be selected. The angular distance from the new centre $\boldsymbol{V}$ to either $\boldsymbol{Q}_{1st}$ and $\boldsymbol{Q}_{2nd}$ is now

$$r_V = \arccos(\boldsymbol{V} \cdot \boldsymbol{Q}_{\mathrm{node}}), \quad \text{with node = 1st or 2nd.} \quad \text{(A14)}$$

Next, it is necessary to check that no new stars (different from the ones at the triangle nodes) have entered within the new circle. This can be computed as

$$r_{V,\mathrm{revised}} = \mathrm{maximum}\left\{r_V, \mathrm{minimum}[\arccos(\boldsymbol{V} \cdot \boldsymbol{S_i})]\right\}, \quad \text{(A15)}$$

where $i = 1, \ldots, N_{\mathrm{stars}}$.

Note that it must also be checked that with this new radius, $r_{V,\mathrm{revised}}$, the circle centred at $\boldsymbol{V}$ is still within the sky subregion. In a similar manner, as discussed in Step 2, the distance from $\boldsymbol{V}$ to $\boldsymbol{K}_{\mathrm{sky}}$ is determined as

$$d_V = \arccos(\boldsymbol{V} \cdot \boldsymbol{K}_{\mathrm{sky}}), \quad \text{(A16)}$$

and then the condition that must be satisfied can be written as

$$d_V + r_{V,\mathrm{revised}} \leq \theta_{\mathrm{max}}. \quad \text{(A17)}$$

If the previous condition does not hold, then the radius of the blank field can be redefined as

$$r_{V,\mathrm{revised2}} = \theta_{\mathrm{max}} - d_V. \quad \text{(A18)}$$

The resulting blank field centred at $\boldsymbol{V}$ will be a better (larger) blank field so far as $r_{V,\mathrm{revised}}$ (or $r_{V,\mathrm{revised2}}$) is larger than $r_{I,\mathrm{enlarged}}$.

Step 2: shift the centre between the incentre and the circumcentre

Independently of the success of the previous step, another possibility worth being explored is shifting the centre of the blank field along the great circle connecting the incentre with the circumcentre, with the constraint that the new circle does not cross the sky subregion boundary (see Fig. A2e).

For this computation, the bisection method can easily be employed. Since the solution for the new centre will be a point in the great circle connecting $\boldsymbol{I}$ with $\boldsymbol{C}$, it is possible to use two auxiliary vectors $\boldsymbol{L}_1$ and $\boldsymbol{L}_2$ which are initialized as $\boldsymbol{L}_1 = \boldsymbol{I}$ and $\boldsymbol{L}_2 = \boldsymbol{C}$. Then, the process enters into an iterative procedure in which the following steps are performed:

(i) The mid-point of the great circle connecting $\boldsymbol{L}_1$ with $\boldsymbol{L}_2$ is determined as

$$\boldsymbol{L}_{\mathrm{mid}} = \frac{\boldsymbol{L_1} + \boldsymbol{L_2}}{||\boldsymbol{L_1} + \boldsymbol{L_2}||}.$$

(ii) The minimum angular distance from the previous point to any of the triangle nodes is evaluated using

$$d_{L-Q} = \mathrm{minimum}[\arccos(\boldsymbol{L}_{\mathrm{mid}} \cdot \boldsymbol{Q}_i)], \quad \text{with } i = 1, 2 \text{ or } 3.$$

(iii) The angular distance from $\boldsymbol{L}_{\mathrm{mid}}$ to the border of the sky subregion is also determined as

$$d_{L-\mathrm{Sky}} = \theta_{\mathrm{max}} - \arccos(\boldsymbol{L}_{\mathrm{mid}} \cdot \boldsymbol{K}_{\mathrm{sky}}).$$

(iv) If the two previous angular distances are equal within a given tolerance (for our purposes, $|d_{L-Q} - d_{L-\mathrm{Sky}}| < 0.01$ arcsec is enough), then the iterative procedure halts and the final result is defined as $\boldsymbol{W} = \boldsymbol{L}_{\mathrm{mid}}$. Otherwise, one of the auxiliary vectors must be redefined according to

$$\text{if } (d_{L-Q} - d_{L-\mathrm{Sky}}) \text{ is } \begin{cases} > 0, & \text{then } \boldsymbol{L}_2 = \boldsymbol{L}_{\mathrm{mid}} \\ < 0, & \text{then } \boldsymbol{L}_1 = \boldsymbol{L}_{\mathrm{mid}} \end{cases}$$

and the process is iterated by repeating steps (i)–(iv).

At the end of the iterative process, a new centre $\boldsymbol{W}$ has been computed (see Fig. A2e), which is equidistant from the nearest triangle node and from the boundary of the sky subregion, that is, $r_W = d_{L-\mathrm{Sky}} = d_{L-Q}$.

Finally, it must be checked that no new stars have entered into the new circle. Similarly to what was carried out in the previous step, the new radius can be refined by using

$$r_{W,\mathrm{revised}} = \mathrm{maximum}\{r_W, \mathrm{minimum}[\arccos(\boldsymbol{W} \cdot \boldsymbol{S}_i)]\} \quad \text{(A19)}$$

where $i = 1, \ldots, N_{\rm stars}$.

It is important to highlight that the new radius $r_{W,\rm revised}$ will not necessarily be larger than the radii previously derived in Steps 1a, 1b and 1c (in fact, the example illustrating this appendix shows that the blank field in Fig. A2d centred at $\boldsymbol{V}$ with radius r_V is larger than the blank field in Fig. A2e centred at $\boldsymbol{W}$ with radius r_W).

Step 3: random search in the intersection between the circumcircle and the sky subregion

A final, but also effective, brute force method consists in using a random search of a valid blank-field centre within the intersection region between the circumcircle and the sky subregion (see Fig. A2f). For this purpose, random points are generated on that region, imposing that any small area has to contain, on average, the same number of points (see e.g. Weisstein 2011). For each random point $\boldsymbol{T}$, the valid blank-field radius is evaluated as

$$r_T = \text{minimum}[\arccos(\boldsymbol{T} \cdot \boldsymbol{S}_i)], \quad \forall i = 1, \ldots, N_{\rm stars}. \tag{A20}$$

It is also necessary to check that the resulting blank field remains inscribed in the sky subregion. For that purpose, the distance from the centre to the border of the subregion is determined using

$$d_T = \arccos(\boldsymbol{T} \cdot \boldsymbol{K}_{\rm sky}), \tag{A21}$$

and the corresponding condition to be verified is

$$d_T + r_T \leq \theta_{\rm max}. \tag{A22}$$

If this is not the case, the value of the radius can be refined using

$$r_{T,\rm refined} = \theta_{\rm max} - d_T. \tag{A23}$$

Obviously, the solution obtained with this method must be compared with the solutions derived in the previous steps in order to decide which one provides the largest blank field in the neighbourhood of the considered boundary triangle.

Successfulness of the different steps

The three steps described above produce different possible valid blank fields associated with each boundary triangle. The adopted valid blank field in each case will be the largest amongst those alternatives.

It is interesting to investigate the successfulness of the three steps providing the largest blank field. As a first-order estimation of these numbers, we have measured the percentage of success of each step when tessellating random stellar fields. Since the success ratio for Step 3 depends on the number of random points drawn within the intersection region between the circumcircle and the sky subregion, we have computed those percentages using different numbers of random points. The results are displayed in Fig. A3. Each colour in this figure indicates a fixed number of random points employed in Step 3. When no random points are used (represented in red colour), the median percentage of success of Steps 1 and 2 is 23 and 77 per cent, respectively. Not surprisingly, these values decrease as the number of random points in Step 3 increases, reaching a stable situation as the number of random points exceeds a few hundreds. In particular, for 10^4 random points, the median percentages of success (represented in magenta colour) are 10, 24 and 66 per cent for Steps 1, 2 and 3, respectively.

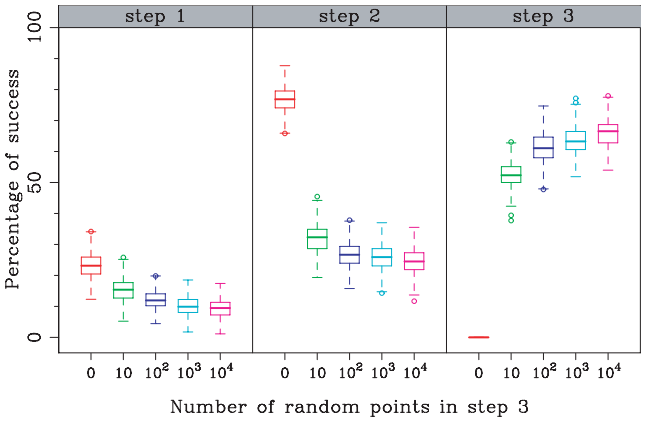

Figure A3. Box-and-whisker plot showing the percentage of success of the different steps described in Appendix A. The bottom and top of each box show the 25th and 75th percentiles, whereas the thick horizontal line marks the median. The whiskers (vertical dashed lines) show 1.5 times the interquartile range. Since each colour represents a fixed number of random points employed in the search for a valid blank-field region in Step 3, the sum of the percentages in the three steps for a fixed colour is 100.

The previous results have shown that although Step 3 will be, in general, responsible for providing the valid blank field, the contribution of the other two steps is not negligible.

This paper has been typeset from a TEX/LATEX file prepared by the author.